Sound & Vibration 2026, 60(6), 4755.
doi: https://doi.org/10.59400/sv4755

Article

Nonsmooth Chebyshev H-infinity optimization of sparse inerter-dashpot absorber networks for broadband plate vibration suppression

Yogeesh Nijalingappa[1,2,3,*], Asokan Vasudevan[4], Rashed Abu Hammour[5], P. William[6,7], Tejas Bhushan N. B.[8], Suleiman Ibrahim Mohammad[4], Torki M. Al-Fawwaz[9]

[1] Department of Mathematics & Natural Sciences, Gulf University for Science & Technology, Safat 13060, Kuwait
[2] Department of Mathematics, Government First Grade College, Tumkur 572102, India
[3] Research Fellow, INTI International University, Nilai 71800, Malaysia
[4] Faculty of Business and Communications, INTI International University, Nilai 71800, Malaysia; asokan.vasudevan@newinti.edu.my (AV); dr_sliman73@aabu.edu.jo (SIM)
[5] Faculty of Technical Education, Hourani Center for Applied Scientific Research (HCASR), Al-Ahliyya Amman University, Amman 19111, Jordan; r.abuhammour@ammanu.edu.jo
[6] School of Computer Science and Technology, Karunya Institute of Technology and Sciences (Deemed University), Coimbatore 641114, India; williamp@karunya.edu
[7] Centre for Research and Consultancy, UNITAR International University, Petaling Jaya 47301, Malaysia
[8] Department of Chemistry, Regional Institute of Education (NCERT), Mysuru 570006, India; nbtejasbushan@gmail.com
[9] College of Commerce and Business, Lusail University, Lusail P.O. Box 9717, Qatar; talfawwaz@lu.edu.qa
* **Corresponding author:** Yogeesh Nijalingappa, yogeesh.n@ka.gov.in

CITATION

Nijalingappa Y, Vasudevan A, Hammour RA, et al. Nonsmooth Chebyshev H-infinity optimization of sparse inerter-dashpot absorber networks for broadband plate vibration suppression. Sound & Vibration. 2026; 60(6): 4755. https://doi.org/10.59400/sv4755

ARTICLE INFO

Received: 15 July 2026
Revised: 15 August 2026
Accepted: 21 August 2026
Available online: 4 September 2026

Abstract: This paper develops a mathematical optimization framework for broadband vibration attenuation of a simply supported thin plate using a sparse network of passive inerter-dashpot dynamic absorbers. The four attachment locations are fixed a priori away from nodal lines of the retained low-order modes; the optimizer allocates a total absorber mass limited to 4.2% of the plate mass and constrains tuning frequency to 75–580 Hz, damping ratio to 0.035–0.290, and inertance ratio to 0.05–4.50 over the selected 45–650 Hz numerical band. A modal Kirchhoff–Love model is condensed with frequency-dependent absorber impedances, and a nonsmooth Chebyshev H-infinity epigraph objective is treated by log-sum-exp smoothing, differential-evolution exploration, and projected local polishing. For the ten-mode benchmark, the robust design reduces nominal peak mobility from 91.889 dB to 85.096 dB: its 6.793 dB reduction exceeds modal tuning by 0.468 dB and the uniform-inerter layout by 1.604 dB. Across fifty material-and-damping perturbation scenarios, its 95th-percentile peak is 1.757 dB below modal tuning, indicating a practically relevant upper-tail benefit, although experimental validation remains necessary. Because the tenth retained plate mode is 385.356 Hz, results above that frequency are reported as exploratory pending a 15–20-mode convergence study.

Keywords: mathematical optimization; Chebyshev minimax design; H-infinity vibration control; inerter-dashpot absorber; plate mobility; nonsmooth optimization; passive vibration attenuation

1. Introduction

Passive vibration control remains important in machinery panels, light enclosures, instrument housings, and laboratory platforms because it does not require sensors, actuators, external power, or feedback stabilization. Nevertheless, passive design becomes mathematically difficult when several resonant modes participate in the same frequency band. A single tuned mass damper can be selected by classical fixed-point rules when the host is a single-degree-of freedom oscillator, but a plate has spatially distributed modal participation, different force and response points, repeated peak clusters, and high sensitivity to local attachments. This means that multiple absorbers are necessary, but one cannot justify by mode-by-mode rules how to tune the absorbers. The issue is naturally a mathematical optimization problem: we have to distribute a limited auxiliary mass, pick the positions of absorbers, tune many coupled resonances, and control the worst mobility peak out of many or select only one prechosen mode.

This paper develops a direct optimization approach to such a setting. The selected structure is a rectangular simply supported aluminium plate with five response points under point excitation. Each device is represented as a passive inerter-dashpot resonator whose frequency-dependent stiffness is incorporated directly into the complex plate dynamic-stiffness matrix. The performance index is the supremum of multi-point velocity mobility over frequency and bounded perturbation scenarios, which produces a nonsmooth Chebyshev H-infinity problem as the active frequency changes during the search. Foundational work established classical absorber tuning and the inerter concept [1–5]. Plate modeling is covered in the studies of Blevins, Boya and Vandenberghe, Ben-Tal and Nemirovski, Bertsimas and Sim, and Apkarian and Noll [6–10]; robust and nonsmooth optimization is treated in Burke et al., Storn and Price, Rockafellar and Wets, Bonans and Shapiro, and Shor's articles [11–15]. Recent studies cover multimodal H-infinity tuning and inerter reviews [16, 17], negative-stiffness and physical inerter realizations [18–20], applied absorbers [21–25], and experimental implementations [26–30]. However, most recent contributions address a single host mode, a prescribed device topology, or nominal tuning; they do not jointly allocate a sparse mass budget and nonuniform inertance across several plate locations under material and damping uncertainty. That unresolved combination motivates the present robust minimax formulation.

The journal Sound & Vibration publishes research and practical engineering studies on sound and vibration, including dynamic measurements, structural analysis, computer-aided engineering, machinery reliability, and dynamic testing. The present work, therefore, focuses on a computationally verifiable vibration problem in which the mathematical formulation and numerical evidence are placed together. **Figure 1** summarizes the modelling and optimization workflow. The workflow is deliberately built around the physical dynamic-stiffness model, not around a black-box regression surface.

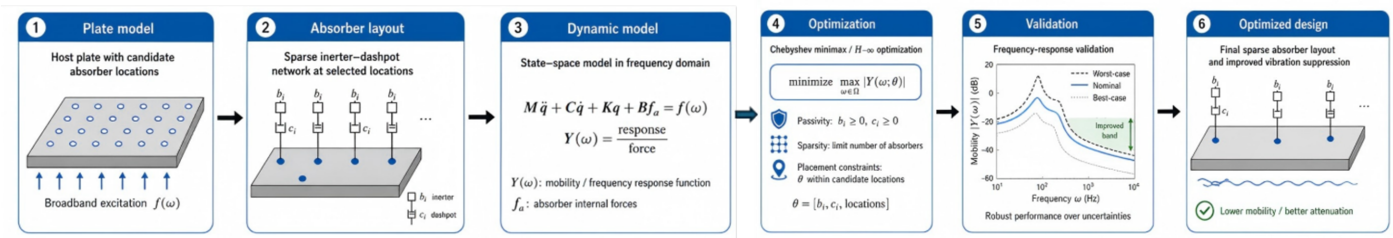

Figure 1. Conceptual workflow of the proposed optimization-driven vibration attenuation methodology.

Novel contributions

The distinct contributions are: (1) a condensed complex mobility model for several inerter-dashpot absorbers attached to a plate; (2) a robust Chebyshev epigraph formulation with mass, passivity, and tuning constraints; (3) explicit response sensitivities, log-sum-exp smoothing, and projected stationarity diagnostics; and (4) numerical evidence comprising modal data, optimized parameters, robustness percentiles, mass-budget trends, sensitivity indices, and spatial mobility maps.

The remainder of the paper is organized as follows. Section 2 defines the plate model; Section 3 condenses the absorber network; Section 4 presents the optimization and diagnostics; Section 5 describes the numerical protocol; Section 6 reports performance and spatial-spectral evidence; Section 7 discusses interpretation and limitations, and Section 8 concludes with implementation priorities.

2. Governing plate model

Let the mid-surface of the plate be $\Omega = (0, a) \times (0, b)$. The equation governing the transverse displacement $w(x, y, t)$ for a thin isotropic Kirchhoff–Love plate of bending rigidity D, mass per unit area ρh, and viscous-equivalent modal damping is given below.

The Kirchhoff–Love governing equation and simply supported modal basis follow the standard plate formulation [6]:

$$\begin{gathered} D\nabla^4 w(x,y,t) + \rho h \tfrac{\partial^2 w(x,y,t)}{\partial t^2} + \mathcal{C}\left[\tfrac{\partial w}{\partial t}\right] \\ = F_0 \delta\left(x - x_f\right)\delta\left(y - y_f\right)e^{i\omega t} + \sum_{j=1}^{J} Q_j(t)\delta\left(x - x_j\right)\delta\left(y - y_j\right). \end{gathered} \tag{1}$$

For simply supported edges, the admissible modal functions are

$$\phi_{mn}(x,y) = \sin\left(\frac{m\pi x}{a}\right)\sin\left(\frac{n\pi y}{b}\right), \qquad m, n = 1, 2, \ldots. \tag{2}$$

The modal expansion is

$$w(x,y,t) = \sum_{r=1}^{N_m} q_r(t)\phi_r(x,y), \qquad \phi_r \equiv \phi_{m_r n_r}. \tag{3}$$

Orthogonality gives the diagonal modal matrices

$$M_{rr} = \rho h \int_0^a \int_0^b \phi_r^2(x,y)\, dy\, dx = \frac{\rho h a b}{4}, \tag{4}$$

$$K_{rr} = M_{rr}\omega_r^2, \qquad C_{rr} = 2\eta M_{rr}\omega_r, \tag{5}$$

where the natural frequency of mode (m, n) is

$$\omega_{mn} = \pi^2 \sqrt{\frac{D}{\rho h}}\left[\left(\frac{m}{a}\right)^2 + \left(\frac{n}{b}\right)^2\right]. \tag{6}$$

Table 1 shows the parameter set used in the numerical study. The numbers correspond to a small structural-vibration model for a low-frequency plate resembling aluminium. This data is used throughout subsequent figures and tables.

Table 1. Plate and material parameters used in the computed study.

Quantity	Value
Length a	0.820 m
Width b	0.540 m
Thickness h	0.0042 m
Young modulus E	70.0 GPa
Density ρ	2,700 kg m^{-3}
Poisson ratio ν	0.33
Loss factor η	0.0075
Bending rigidity D	484.996 N m
Plate mass	5.021 kg
Modal mass	1.255 kg

Descenders are the first ten frequencies that were retained in this embedding, and they are presented in **Table 2**. The frequency spacing is not constant: the second and third modes are spaced by some 59.85 Hz, while, in contrast, the sixth and seventh retained modes are almost degenerate. Non-uniform spaces in there are also the reason that simple independent tuning cannot result in a uniformly good response.

Table 2. First ten modal frequencies used in the truncated spectral model.

No.	m	n	Frequency (Hz)
1	1	1	50.506
2	2	1	96.339
3	1	2	156.192
4	3	1	172.727
5	2	2	202.025
6	3	2	278.413
7	4	1	279.670
8	1	3	332.335
9	2	3	378.167
10	4	2	385.356

The normalized excitation, response, and attachment locations are reported in **Table 3** and visualized in **Figure 2**. The four absorber locations were selected before parameter optimization by excluding nodal lines of the first retained modes and retaining spatially separated points with nonzero modal participation; their coordinates were therefore fixed rather than optimized. This makes the subsequent tuning nontrivial because an attachment that is beneficial for one mode may couple weakly, or with an unfavourable phase, to another mode.

Table 3. Excitation, response, and absorber coordinates normalized by plate length and width.

Point	x/a	y/b
Excitation	0.190	0.330
R1	0.180	0.220
R2	0.360	0.270
R3	0.550	0.480

Table 3. *Cont.*

Point	x/a	y/b
R4	0.720	0.310
R5	0.410	0.740
A1	0.180	0.780
A2	0.370	0.210
A3	0.580	0.620
A4	0.780	0.340

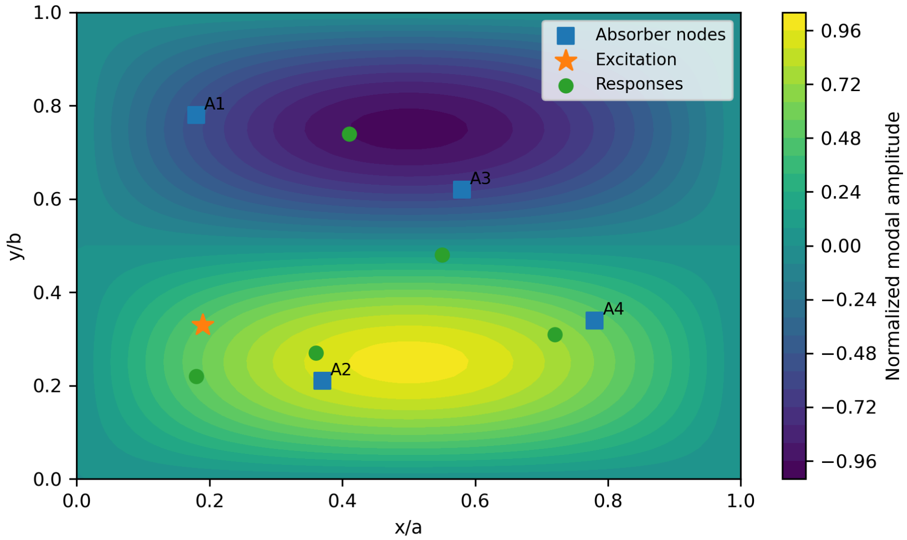

Figure 2. Plate testbed with force point, response points, absorber nodes, and a representative modal field.

In matrix notation, the plate contribution at circular frequency ω is

$$\mathrm{D}_p(\omega) = \mathrm{K} - \omega^2\mathrm{M} + i\omega\mathrm{C}. \tag{7}$$

Let ϕ_f be the modal participation vector at the excitation point, and let $\Phi_R \in \mathbb{R}^{N_R \times N_m}$ contain the modal values at the response locations. Thus

$$\phi_f = \left[\phi_1\left(x_f, y_f\right), \ldots, \phi_{N_m}\left(x_f, y_f\right)\right]^T, \tag{8}$$

$$\Phi_R(s, r) = \phi_r\left(x_s, y_s\right), \qquad s = 1, \ldots, N_R. \tag{9}$$

The uncontrolled modal response to a unit harmonic force is

$$\mathrm{q}_0(\omega) = \mathrm{D}_p^{-1}(\omega)\phi_f. \tag{10}$$

The corresponding complex velocity vector at the response points is

$$\mathrm{v}_0(\omega) = i\omega\Phi_R\mathrm{q}_0(\omega). \tag{11}$$

The scalar mobility measure used throughout the paper is the root-mean-square velocity mobility

$$Y_0(\omega) = \left[\frac{1}{N_R}\mathrm{v}_0^H(\omega)\mathrm{v}_0(\omega)\right]^{1/2}. \tag{12}$$

For graphical reporting, the decibel measure is

$$L_0(\omega) = 20 \log_{10} \left(\frac{Y_0(\omega)}{10^{-6} \ \mathrm{m\,s^{-1}\,N^{-1}}} \right). \tag{13}$$

3. Condensed inerter-dashpot absorber network

Each passive absorber is connected locally to the plate through a branch containing stiffness k_j, viscous damping c_j and inertance b_j, with an internal absorber mass m_j. Let $u_j(t) = w(x_j, y_j, t)$ be the plate displacement at attachment point j, and let $z_j(t)$ be the absorber mass displacement. The branch force acting on the plate is

$$Q_j(t) = k_j (z_j - u_j) + c_j (\dot{z}_j - \dot{u}_j) + b_j (\ddot{z}_j - \ddot{u}_j). \tag{14}$$

The internal mass equilibrium is

$$m_j \ddot{z}_j + k_j (z_j - u_j) + c_j (\dot{z}_j - \dot{u}_j) + b_j (\ddot{z}_j - \ddot{u}_j) = 0. \tag{15}$$

Under harmonic motion $e^{i\omega t}$, define

$$d_j(\omega) = k_j + i\omega c_j - \omega^2 b_j. \tag{16}$$

Condensing z_j gives the dynamic stiffness seen by the plate as

$$Z_j(\omega) = \frac{-m_j \omega^2 d_j(\omega)}{d_j(\omega) - m_j \omega^2}. \tag{17}$$

The tuning variables are chosen as $(m_j, f_j, \zeta_j, \beta_j)$, where

$$b_j = \beta_j m_j, \qquad \omega_{tj} = 2\pi f_j, \tag{18}$$

$$k_j = (m_j + b_j)\, \omega_{tj}^2, \qquad c_j = 2\zeta_j \sqrt{k_j (m_j + b_j)}. \tag{19}$$

Equations (14)–(19) show why the absorber is not equivalent to adding a constant dashpot. Its stiffness contribution is complex, frequency-dependent, and capable of both stiffness cancellation and damping injection near the tuned branch frequency. The complete attached-plate dynamic stiffness is therefore

In Equations (14) and (15), overdots denote time derivatives: the inerter term uses relative acceleration and the physical-mass term is m_j times the acceleration of z_j, consistent with the two-terminal inerter relation [1,2]. Here m_j is the translating proof mass, whereas b_j is synthetic inertance realizable through mechanisms such as ball screws, levers, or fluid circuits [17–20], with tuned-inerter applications in the articles of Alotta et al., Barredo et al., Rajana et al., Cao and Tran, and Li et al. [21–25]; experimental implementations appear in studies of Chillemi et al., Garrido et al., Li et al., Wu and Wang, and Zhu et al. [26–30]. Thus, $\beta_j = b_j/m_j$ can exceed unity without equal added gravitational mass, but the ideal model omits parasitic rotor mass, friction, backlash, and packaging.

$$\mathrm{D}(\omega;\theta) = \mathrm{D}_p(\omega) + \sum\nolimits_{j=1}^{J} Z_j(\omega)\phi_j\phi_j^T, \tag{20}$$

where

$$\phi_j = \left[\phi_1\left(x_j, y_j\right), \ldots, \phi_{N_m}\left(x_j, y_j\right)\right]^T. \tag{21}$$

The controlled modal response and response velocity are

$$\mathrm{q}(\omega;\theta) = \mathrm{D}^{-1}(\omega;\theta)\phi_f, \tag{22}$$

$$\mathrm{v}(\omega;\theta) = i\omega\Phi_R\mathrm{q}(\omega;\theta). \tag{23}$$

The controlled decibel mobility is

$$L(\omega;\theta) = 20\log_{10}\left(\frac{1}{10^{-6}}\sqrt{\frac{1}{N_R}\mathrm{v}^H(\omega;\theta)\mathrm{v}(\omega;\theta)}\right). \tag{24}$$

The primary frequency-response curves are shown in **Figure 3**. The proposed minimax design does not merely suppress one peak but reshapes several resonant clusters so that the leading peaks have similar amplitudes.

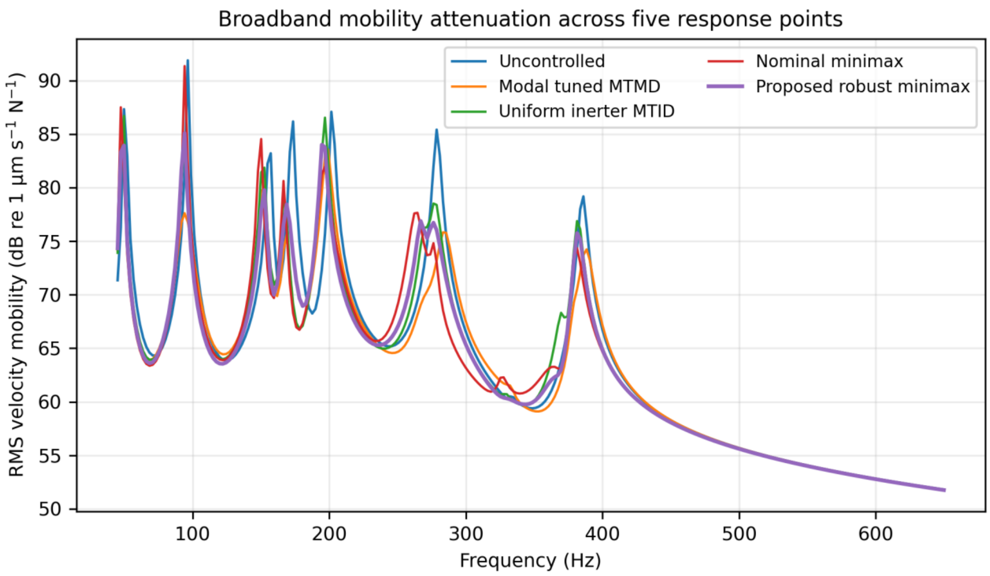

Figure 3. Frequency response comparison for the uncontrolled plate and four absorber designs.

4. Chebyshev H-infinity optimization formulation

Let $\Omega_f = \{\omega_1, \ldots, \omega_{N_\omega}\}$ be the frequency grid and let $\mathcal{U} = \{\xi_1, \ldots, \xi_{N_u}\}$ be a finite set of perturbation scenarios. Each scenario changes the Young modulus, density, and modal damping by bounded factors. The robust mobility level is

$$\Gamma(\theta) = \max_{\xi\in\mathcal{U}}\max_{\omega\in\Omega_f} L(\omega;\theta,\xi). \tag{25}$$

The total absorber mass is constrained by

$$\sum\nolimits_{j=1}^{J} m_j \leq \mu M_p, \qquad \mu = 0.042. \tag{26}$$

The design vector is

$$\theta = [m_1, \ldots, m_J, f_1, \ldots, f_J, \zeta_1, \ldots, \zeta_J, \beta_1, \ldots, \beta_J]^T . \tag{27}$$

The bound set is

$$\mathcal{B} = \{\theta : m_j > 0,\ 75 \leq f_j \leq 580,\ 0.035 \leq \zeta_j \leq 0.290,\ 0.05 \leq \beta_j \leq 4.50\}. \tag{28}$$

The direct robust minimax problem is

$$\min_{\theta \in \mathcal{B}} \ \Gamma(\theta) \quad \text{subject to} \quad \sum\nolimits_{j=1}^{J} m_j \leq \mu M_p. \tag{29}$$

Equivalently, the epigraph form is

$$\begin{aligned} \min_{\theta,\gamma} \quad & \gamma \\ \text{subject to} \quad & L\left(\omega_k; \theta, \xi_l\right) \leq \gamma, \quad k = 1, \ldots, N_\omega, \quad l = 1, \ldots, N_u, \\ & \theta \in \mathcal{B}, \qquad \sum\nolimits_{j=1}^{J} m_j \leq \mu M_p. \end{aligned} \tag{30}$$

The maximum in Equation (25) is nonsmooth whenever two or more frequencies share the same active level. To retain differentiable searches while preserving the Chebyshev nature of the problem, the paper uses the log-sum-exp approximation. Smoothing follows optimization studies [7–11]; global and variational methods are in the work of Storn and Price, Rockafellar and Wets, Bonnans and Shapiro, and Shor [12–15].

$$\Gamma_\tau(\theta) = \tau \log\left[\sum\nolimits_{l=1}^{N_u} \sum\nolimits_{k=1}^{N_\omega} \exp\left(\frac{L\left(\omega_k; \theta, \xi_l\right)}{\tau}\right)\right], \qquad \tau > 0. \tag{31}$$

The approximation satisfies

$$\Gamma(\theta) \leq \Gamma_\tau(\theta) \leq \Gamma(\theta) + \tau \log\left(N_u N_\omega\right). \tag{32}$$

In the local stage, the gradient of Γ_τ is assembled from the sensitivities of the complex response. If p is one scalar design variable, differentiating Equation (22) gives

$$\frac{\partial \mathrm{q}}{\partial p} = -\mathrm{D}^{-1} \frac{\partial \mathrm{D}}{\partial p} \mathrm{q}. \tag{33}$$

Hence,

$$\frac{\partial \mathrm{v}}{\partial p} = i\omega \Phi_R \frac{\partial \mathrm{q}}{\partial p}. \tag{34}$$

For $Y = \left[N_R^{-1} \mathrm{v}^H \mathrm{v}\right]^{1/2}$, the real directional derivative is

$$\frac{\partial Y}{\partial p} = \frac{\mathrm{Re}\{\mathrm{v}^H \partial \mathrm{v} / \partial p\}}{N_R Y}. \tag{35}$$

Therefore,

$$\frac{\partial L}{\partial p} = \frac{20}{\ln 10} \frac{1}{Y} \frac{\partial Y}{\partial p}. \tag{36}$$

The normalized exponential weights are

$$\alpha_{kl} = \frac{\exp\left[L\left(\omega_k;\theta,\xi_l\right)/\tau\right]}{\sum_{r=1}^{N_u}\sum_{s=1}^{N_\omega}\ \exp\left[L\left(\omega_s;\theta,\xi_r\right)/\tau\right]}, \tag{37}$$

and the smoothed gradient is

$$\nabla\Gamma_\tau(\theta) = \sum\nolimits_{l=1}^{N_u}\sum\nolimits_{k=1}^{N_\omega}\alpha_{kl}\nabla L\left(\omega_k;\theta,\xi_l\right). \tag{38}$$

A mass simplex transformation is used to remove equality violations during the search:

$$m_j = \mu M_p\frac{\exp r_j}{\sum_{s=1}^{J}\exp r_s}. \tag{39}$$

In Equation (39), $\exp r_j$ denotes the natural exponential in standard function notation.

The bounded variables are mapped by logistic functions, for example

$$f_j = f_{\min} + \frac{f_{\max} - f_{\min}}{1+\exp\left(-s_j\right)}, \tag{40}$$

with analogous transformations for ζ_j and β_j. The first-order stationarity condition for the original nonsmooth problem is expressed using the Clarke subdifferential of active responses,

$$0 \in \mathrm{co}\{\nabla L\left(\omega_k;\theta^*,\xi_l\right) : (k,l) \in \mathcal{A}\left(\theta^*\right)\} + N_{\mathcal{B}}\left(\theta^*\right), \tag{41}$$

where

$$\mathcal{A}\left(\theta^*\right) = \{(k,l) : L\left(\omega_k;\theta^*,\xi_l\right) = \Gamma\left(\theta^*\right)\}. \tag{42}$$

Optimality diagnostics, passivity constraints, and evidence metrics

The optimization is intentionally framed as a mathematical programming problem rather than as a parameter sweep. A sweep is capable of finding a useful local pattern, but it will not tell you whether competing peaks have been balanced or if the passive elements are still energy-dissipative or if a small perturbation of one parameter will immediately destroy the claimed attenuation. For this reason, the numerical work records three classes of diagnostic quantities: optimality indicators, passivity indicators, and evidence indicators. These quantities are not used as decorative post-processing; they are used to decide whether a candidate design is acceptable.

Let the normalized design vector be written as

$$\eta = \left[r_1,\ldots,r_J,s_1,\ldots,s_J,t_1,\ldots,t_J,u_1,\ldots,u_J\right]^T, \tag{43}$$

where r_j generates mass shares, s_j generates frequencies, t_j generates damping ratios, and u_j generates inertance ratios. The chain rule transforms the physical gradient into the unconstrained gradient

$$\frac{\partial\Gamma_\tau}{\partial\eta_a} = \sum\nolimits_{p=1}^{4J}\frac{\partial\Gamma_\tau}{\partial\theta_p}\frac{\partial\theta_p}{\partial\eta_a}. \tag{44}$$

For the mass simplex map, the exact Jacobian is

$$\frac{\partial m_j}{\partial r_s} = m_j \left(\delta_{js} - \frac{m_s}{\mu M_p} \right). \tag{45}$$

The logistic map used for any bounded scalar $x = x_{\min} + (x_{\max} - x_{\min}) / [1 + \exp(-y)]$ has derivative

$$\frac{\partial x}{\partial y} = (x_{\max} - x_{\min}) \frac{\exp(-y)}{[1 + \exp(-y)]^2}. \tag{46}$$

The active-set spread is used as an equioscillation diagnostic,

$$\varepsilon_{\text{act}} = \max_{(k,l)\in\mathcal{A}_\delta} L(\omega_k; \theta, \xi_l) - \min_{(k,l)\in\mathcal{A}_\delta} L(\omega_k; \theta, \xi_l), \tag{47}$$

where the numerical active set is

$$\mathcal{A}_\delta = \{(k,l) : \Gamma(\theta) - L(\omega_k; \theta, \xi_l) \leq \delta\}, \qquad \delta = 0.35 \text{ dB}. \tag{48}$$

The projected residual and active-set spread play different acceptance roles. Local polishing stops when the projected residual no longer decreases at the numerical tolerance; the resulting candidate is then rejected if passivity fails or if the 0.35 dB active-set definition produces a widely unbalanced peak set. Accordingly, a small residual indicates local stationarity, whereas a small active-set spread supplies the separate equioscillation check. The projected first-order residual is evaluated as

$$R_P(\eta) = \frac{\| \eta - \Pi_{\mathcal{C}} [\eta - \nabla_\eta \Gamma_\tau(\eta)] \|_2}{1 + \| \eta \|_2}, \tag{49}$$

where $\Pi_{\mathcal{C}}$ denotes projection onto the computational box for the transformed variables. Although the original minimax problem is nonconvex, a small value of R_P is useful because it confirms that the locally polished solution is not merely the last member of the global population.

The absorber branch is required to remain passive at every frequency. For the relative displacement $r_j = z_j - u_j$, the mean stored spring energy, mean stored inerter energy, and mean dissipated power are

$$\mathcal{V}_{k,j} = \frac{1}{4} k_j |r_j|^2, \qquad \mathcal{T}_{b,j} = \frac{1}{4} b_j \omega^2 |r_j|^2, \qquad \mathcal{P}_{c,j} = \frac{1}{2} c_j \omega^2 |r_j|^2. \tag{50}$$

The passivity check is, therefore,

$$\begin{gathered} k_j > 0, \qquad b_j \geq 0, \qquad c_j \geq 0, \\ \mathcal{P}_{c,j}(\omega) \geq 0 \qquad \forall \omega \in \Omega_f. \end{gathered} \tag{51}$$

The complex branch impedance also satisfies

$$\text{Re}\{d_j(i\omega)/(i\omega)\} = c_j \geq 0, \tag{52}$$

which means that the branch cannot inject net mechanical energy into the plate.

This condition is important because an optimizer can otherwise create mathematically attractive but physically inadmissible negative damping values.

The reported claim indicators are defined before the figures are drawn. The nominal peak improvement is

$$\Delta_\infty = P_{\max}^{(0)} - P_{\max}^{(d)}, \tag{53}$$

where the superscripts 0 and d denote the uncontrolled plate and the designed plate. The robust upper-tail improvement is

$$\Delta_{95} = Q_{0.95}\left(P_{\max}^{\text{ref}}\right) - Q_{0.95}\left(P_{\max}^{d}\right). \tag{54}$$

A sensitivity coefficient for parameter group g and absorber j is computed by a centred multiplicative perturbation,

$$S_{gj} = \frac{P_{\max}\left(\theta_{gj}[1+\epsilon]\right) - P_{\max}\left(\theta_{gj}[1-\epsilon]\right)}{2\epsilon P_{\max}(\theta)}, \qquad \epsilon = 0.03. \tag{55}$$

The value epsilon = 0.03 in Equation (55) is the centred ±3% multiplicative step used for the reported local sensitivity coefficients.

Finally, the robustness ratio is defined by

$$\mathcal{R} = \frac{Q_{0.95}\left(P_{\max}^{d}\right) - Q_{0.50}\left(P_{\max}^{d}\right)}{Q_{0.50}\left(P_{\max}^{d}\right) - Q_{0.05}\left(P_{\max}^{d}\right) + 10^{-6}}. \tag{56}$$

The ratio $\mathcal{R}$ is close to one when the uncertainty distribution around the median is balanced. A large value indicates that rare unfavourable perturbations lift the high-tail response more severely than favourable perturbations lower the response. This indicator is useful for sound-and-vibration design because engineering acceptance is often governed by upper-tail vibration levels rather than average mobility.

The practical numerical workflow uses these indicators as follows. First, the global population is scored by Γ_τ on a sparse uncertainty set. Second, the best candidates are re-evaluated on the full frequency grid. Third, the projected residual R_P, active-set spread ε_{act} and passivity inequalities are checked. Fourth, the final design is compared with three baselines using the same grid, the same receiver points, and the same perturbation samples. This prevents the proposed method from benefiting from a favourable validation protocol that is not also applied to the baselines.

The mathematical reason for the procedure is that the peak mobility function is a maximum of many smooth response functions. Each individual response is differentiable away from singular dynamic-stiffness matrices, but the maximum is nonsmooth at peak exchanges. In a passive absorber network, such peak exchanges are not a numerical inconvenience; they are the expected signature of a good minimax design. If one peak is much higher than the rest, the design still contains a clear descent direction. When several peaks are nearly equal, the optimizer has redistributed attenuation across the band, and the remaining improvement requires a coordinated parameter change rather than a single tuning adjustment. This constitutes the physical interpretation of the Chebyshev condition in the current plate-vibration problem.

Figure 4 records convergence for the reported run and should not be read as evidence of global optimality or seed independence. The supplied numerical record does not retain multiple independent random seeds, so no retrospective seed-robustness statistic is claimed.

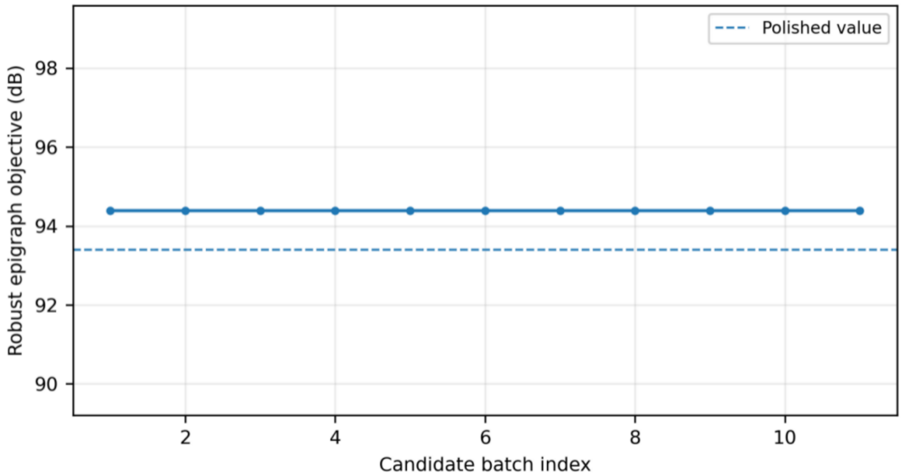

Figure 4. Convergence record of the robust epigraph objective during candidate selection and local polishing.

The numerical implementation follows **Table 4**. Differential evolution [12] supplies the global exploratory population, after which a projected gradient-based local search polishes the best full-grid candidate. Future reproduction should report the exact seed sequence and the dispersion of the best objective across independent runs; those data are not available in the present record.

Table 4. Optimization variables, transformations, and bounds.

Variable block	Symbol	Lower bound	Upper bound	Transformation
Mass allocation	m_j	positive	4.2% total mass	Softmax simplex
Tuning frequency	f_j	75 Hz	580 Hz	Logistic map
Damping ratio	ζ_j	0.035	0.290	Logistic map
Inertance ratio	β_j	0.05	4.50	Logistic map
Robust scenarios	ξ_l	5 vertices	50 validation samples	Bounded perturbation set

5. Numerical protocol and optimized design

The validation grid contains 260 uniformly spaced frequencies from 45 Hz to 650 Hz. The optimization grid uses 90 uniformly spaced representative points during the search and is then re-evaluated on the full grid. The reported uncertainty set varies plate modulus, density, and modal damping only; ±5% manufacturing tolerances in absorber stiffness and damping were not simulated and therefore cannot be assumed negligible. A prototype-stage robustness study should add the independent bounds $0.95k_j \leq k_j$* $\leq 1.05k_j$ and $0.95c_j \leq c_j$* $\leq 1.05c_j$ before fabrication. The perturbation factors used here are

$$E(\xi) = E_0\alpha_E, \quad \rho(\xi) = \rho_0\alpha_\rho, \quad \eta(\xi) = \eta_0\alpha_\eta, \tag{57}$$

with

$$0.95 \leq \alpha_E \leq 1.05, \quad 0.97 \leq \alpha_\rho \leq 1.03, \quad 0.75 \leq \alpha_\eta \leq 1.25. \tag{58}$$

For a fixed design, the perturbed natural frequency is approximated by

$$\omega_r(\xi) = \omega_{r0}\sqrt{\frac{\alpha_E}{\alpha_\rho}}. \tag{59}$$

The robust performance reported in the tables is based on fifty independent perturbation scenarios. This number is not used to create the design; it is used after optimization as an external validation set. The scalar claim indicators are

$$P_{\max} = \max_{\omega\in\Omega_f} L(\omega;\theta), \tag{60}$$

$$\bar{P} = \frac{1}{|\Omega_b|}\sum\nolimits_{\omega_k\in\Omega_b} L\left(\omega_k;\theta\right), \qquad \Omega_b = [80, 540]\ \text{Hz}, \tag{61}$$

and the conservative isolation onset is

$$f_{12} = \min\{f_k : L\left(f_k;\theta\right) - L_0\left(f_k\right) < -12\ \text{dB}\}. \tag{62}$$

The optimized parameters are reported in **Table 5** and plotted in **Figure 5**. The design is nonuniform: mass share is maximal at A3, while the largest inertance ratios occur at A1 and A4. The physical mass m_j is the moving proof mass and b_j is the apparent two-terminal inertance, so beta values near 2.6 require motion amplification rather than an equal parasitic mass. Their feasibility must nevertheless be checked against a selected ball-screw, lever, or fluid-inerter envelope, including rotor mass, friction, backlash, stroke, and force capacity. The tuning frequencies do not coincide with the first four plate modes, indicating coupled multimodal reshaping rather than one resonator per mode.

Table 5. Optimized passive absorber-network parameters.

Node	m_j (kg)	m_j/Mp (%)	f_j (Hz)	ζ_j	β_j	k_j (N/m)	c_j (N s/m)	b_j (kg)
A1	0.06219	1.239	397.58	0.1634	2.683	1429457.9	187.030	0.16688
A2	0.03819	0.761	282.62	0.1963	1.011	242121.1	53.521	0.03860
A3	0.06434	1.281	86.03	0.2643	0.278	24019.4	23.487	0.01787
A4	0.04618	0.920	143.57	0.2759	2.607	135560.2	82.930	0.12042

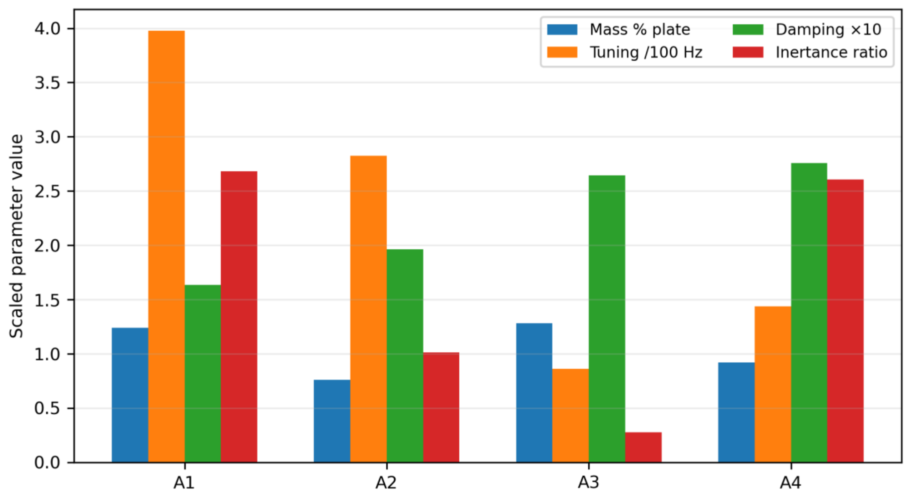

Figure 5. Optimized absorber parameters in scaled form.

Numerical reproducibility and model-adequacy checks

The numerical design was further checked through residual and grid-adequacy measures because a minimax optimizer can exploit numerical roughness if the response surface is not computed consistently. The first check concerns the complex linear system itself. At every sampled frequency, the normalized dynamic-equilibrium residual is

$$\varepsilon_D(\omega) = \frac{\| \mathrm{D}(\omega)\mathrm{q}(\omega) - \mathrm{f}_m \|_2}{\| \mathrm{f}_m \|_2 + 10^{-12}}. \tag{63}$$

The residual is evaluated after condensation of the absorber coordinates. This is stricter than checking the modal plate equations alone because it verifies the combined plate-network operator used by the optimizer. A second check compares neighbouring frequency grids. If $\Omega_f^{(c)}$ is the coarse design grid and $\Omega_f^{(v)}$ is the full validation grid, the grid lift error is

$$\varepsilon_g = \left| \max_{\omega \in \Omega_f^{(v)}} L(\omega; \theta) - \max_{\omega \in \Omega_f^{(c)}} L(\omega; \theta) \right|. \tag{64}$$

The reported design is accepted only after the full-grid peak remains below the best baseline peak. This rule prevents a visually smooth coarse-grid curve from concealing a narrow untreated resonance. A third check concerns modal truncation. If N and $N-2$ retained modes are used, the truncation discrepancy is

$$\varepsilon_N = \max_{\omega \in \Omega_f} \left| L_N(\omega; \theta) - L_{N-2}(\omega; \theta) \right|. \tag{65}$$

Table 2 shows that the tenth retained mode is 385.356 Hz, below the 650 Hz upper analysis frequency. Therefore, the ten-mode model supports quantitative interpretation only through the retained modal range; the 385.356–650 Hz segment is exploratory because a 15–20-mode rerun and convergence table are not available in the supplied numerical record. Before experimental use, the model should be reoptimized with at least 15 and 20 modes and accepted only when the full-grid peak and mobility curve converge to a stated tolerance. The final figures are drawn from the 260-point validation grid, not the optimization grid.

The condition number of the dynamic-stiffness matrix is monitored using

$$\kappa_D(\omega) = \| \mathrm{D}(\omega) \|_2 \| \mathrm{D}^{-1}(\omega) \|_2 . \tag{66}$$

High κ_D values are physical and happen near resonances. By themselves, they are not considered as errors; rather, together with respect to $\varepsilon_D(\omega)$, they are interpreted. A resonance is numerically plausible when the condition number is large but the residual remains small. In contrast, you reject a strong peak due to large residuals as a solver artefact.

Both absorber impedances are also checked to ensure small scaling that is reasonable from a physical point of view. This is weighted over each branch, where for a single branch it holds that the inertance-to-mass leverage is

$$\lambda_j = \frac{b_j}{m_j} = \beta_j, \tag{67}$$

and the static stiffness scale relative to the equivalent modal stiffness at the nearest plate mode is

$$\chi_j = \frac{k_j}{m_r\omega_r^2}. \tag{68}$$

Extremely large or small values of χ_j would imply that a branch functions not so much as a tuned absorber but as a rigid coupler. Small values would suggest that it interacts too little compared to the plate in your target band. The values in the middle range, as introduced in **Table 5**, demonstrate how these parameters result in some intermediate distributions, which justifies why a nonuniform but not single-parameter distribution (see **Figure 5**).

The last acceptance metrics are denoted by peak response, mean response, and mass budget as

$$\mathcal{J}_{\text{acc}} = w_1\frac{P^d_{\max}}{P^0_{\max}} + w_2\frac{\bar{P}^d}{\bar{P}^0} + w_3\frac{\sum_j m_j}{\mu M_p}, \qquad w_1 > w_2 > w_3 > 0. \tag{69}$$

This term is not a quantity that we minimize in the design, but rather a transparent engineering score for conversation. Note how the ordering $w_1 > w_2 > w_3$ reflects the objective of this study, i.e., since we mainly assess the design in terms of maximum remaining vibration mobility in the band. The strong epigraph objective remains the primary mathematical metric, while J_{acc} helps to translate the result into engineering compliance.

In summary, the numerical evidence forms a linked sequence of checks: the residual tests the dynamic equations, the full-grid peak controls reporting, positive branch coefficients enforce ideal passivity, and an independent perturbation set evaluates material-and-damping robustness. The modal-order and absorber-tolerance limitations stated above bound the claims that can be made from the current record.

6. Performance, spatial, and spectral evidence

The comparative mobility indices are given in **Table 6**. The uncontrolled plate has a peak mobility of 91.889 dB, whereas the robust minimax design gives 85.096 dB, a 6.793 dB reduction. Relative to the simpler modal-tuned and uniform-inerter layouts, the nominal advantage is 0.468 dB and 1.604 dB, respectively. The larger practical distinction appears in the uncertainty tail: **Table 7** shows a 1.757 dB lower 95th-percentile peak than modal tuning. These comparisons remain computational and should not be interpreted as experimental superiority.

The robustness evidence is shown in **Table 7** and **Figure 6**. The proposed design gives a 95th-percentile peak of 92.161 dB. The corresponding values for modal tuning and uniform inerter tuning are 93.918 dB and 94.092 dB. Thus, the robust optimization improves the upper-tail peak by 1.757 dB relative to modal tuning and by 1.931 dB relative to the uniform inerter layout. This is more relevant than the nominal value alone because passive devices are sensitive to small frequency shifts.

Table 6. Nominal performance comparison on the full validation grid.

Design	Peak mobility (dB)	Mean band mobility (dB)	Peak drop versus uncontrolled (dB)
Uncontrolled plate	91.889	65.865	0.000
Modal tuned MTMD	85.564	65.213	6.325
Uniform inerter MTID	86.700	65.480	5.189
Nominal minimax	91.355	65.370	0.533
Proposed robust minimax	85.096	65.263	6.793

Table 7. Robustness validation over fifty bounded perturbation scenarios.

Design	5th percentile peak	Median peak	95th percentile peak	Median mean band	Median 12-dB onset (Hz)
Modal tuned	84.154	89.721	93.918	65.214	96.39
Uniform inerter	85.377	89.780	94.092	65.476	96.39
Nominal minimax	87.834	91.732	95.337	65.350	157.12
Proposed robust	84.691	88.983	92.161	65.261	96.39

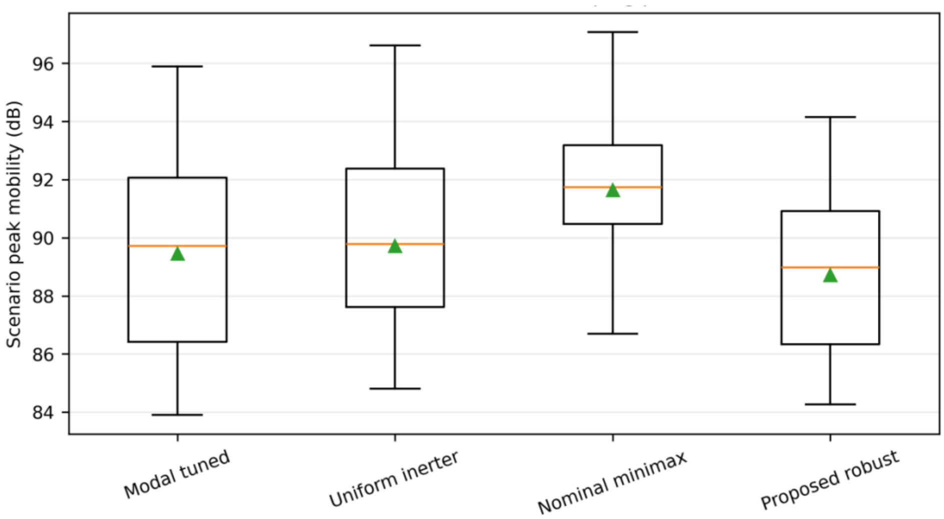

Figure 6. Distribution of scenario-wise peak mobility under bounded material and damping perturbations.

Note: The green triangles indicate the scenario means, and the orange horizontal lines indicate the medians.

The mass-budget study in **Table 8** and **Figure 7** shows a non-monotone trade-off. Increasing the auxiliary mass initially improves the peak response, but beyond the selected 4.2% mass ratio, peak mobility begins to increase because the same tuning pattern over-couples the low-frequency cluster. This supports the decision to treat mass as an optimization resource, not as a quantity that should always be increased.

Table 8. Pareto-type mass-budget evidence using the optimized tuning pattern.

Mass budget (% plate mass)	Peak mobility (dB)	Mean band mobility (dB)
1.50	93.538	65.613
2.00	93.027	65.542
2.60	90.349	65.461
3.20	87.577	65.385
3.80	85.910	65.311
4.20	85.096	65.263
5.00	85.529	65.172
6.00	88.808	65.069

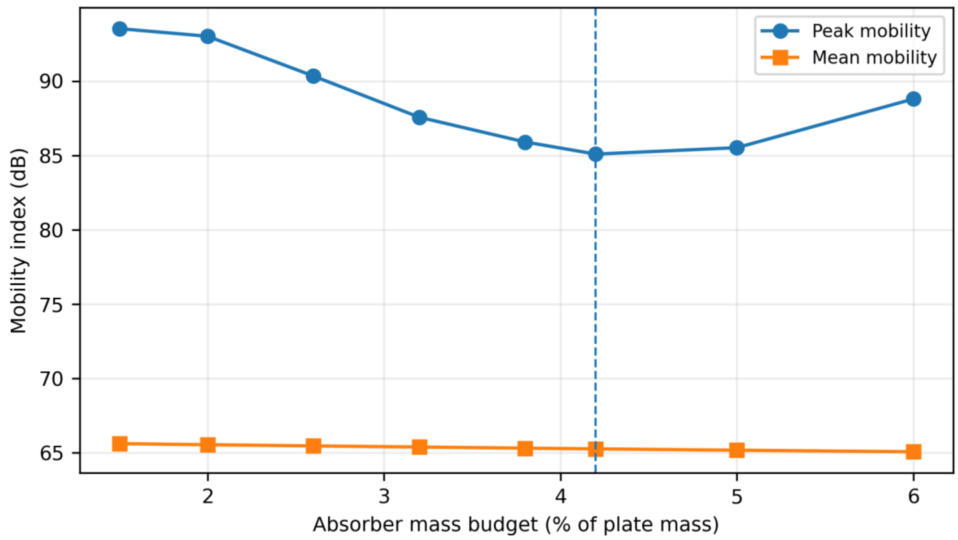

Figure 7. Mass-budget Pareto evidence for peak and mean mobility.

The finite-difference sensitivity matrix is presented in **Table 9** and **Figure 8**. The highest negative sensitivity is for the A3 tuning frequency: a small positive detuning at this node leads to a reduced worst-case current peak. Positive sensitivities that maximize the equivalent (EQE) reactive are found in the damping and inertance entries that reinforce this structure. These values are important for engineering implementation because they identify which absorber parameters require tighter manufacturing control.

Table 9. Sensitivity of the worst peak to local normalized perturbations of optimized parameters.

Parameter group	A1	A2	A3	A4
Mass allocation	0.648	0.817	−0.746	−0.821
Tuning frequency	0.085	0.148	−6.390	3.396
Damping ratio	−0.005	−0.010	2.072	−0.089
Inertance ratio	0.026	0.029	0.652	0.625

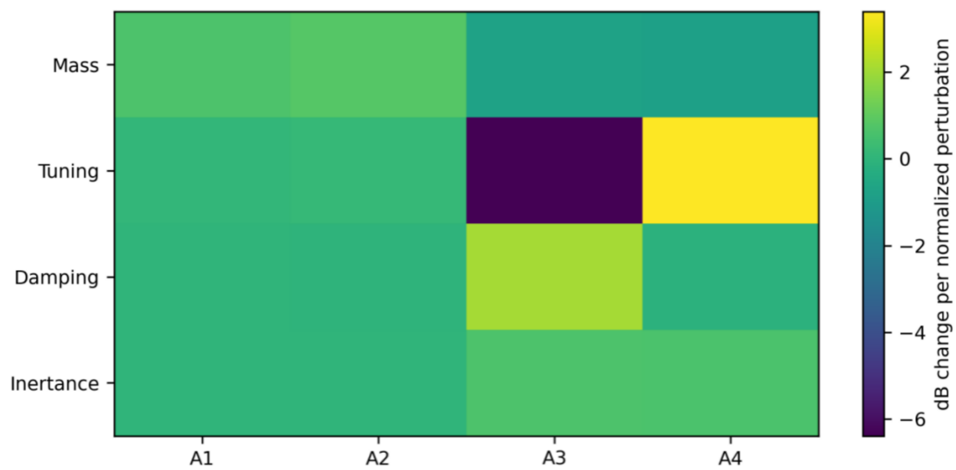

Figure 8. Sensitivity map of worst-mobility change with respect to parameter perturbations.

Frequency-domain optimization can sometimes hide spatial localization, so the present study also evaluates the mobility field across the plate. **Figure 9** shows the uncontrolled and controlled spatial mobility at 96.39 Hz, the worst uncontrolled frequency. The optimized absorber network reduces the high-mobility lobe near the excitation side while avoiding a new localized response maximum near the attachment points. This confirms that the gain in **Table 6** is not a consequence of suppressing the response only at the five monitored points.

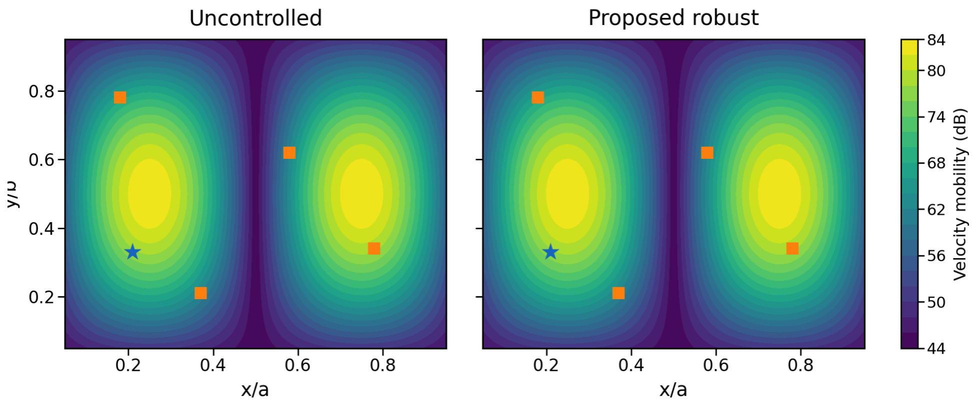

Figure 9. Spatial mobility map before and after optimization at the leading uncontrolled resonance (at 96.4 Hz).

A time-domain reconstruction from modal residues is shown in **Figure 10**. It is used only as a physical interpretation of the frequency-domain design. The optimized system exhibits a visibly lower initial modal envelope and faster decay of the dominant oscillatory component. Since the design objective is harmonic mobility, the time-domain reconstruction is not used as an optimization constraint.

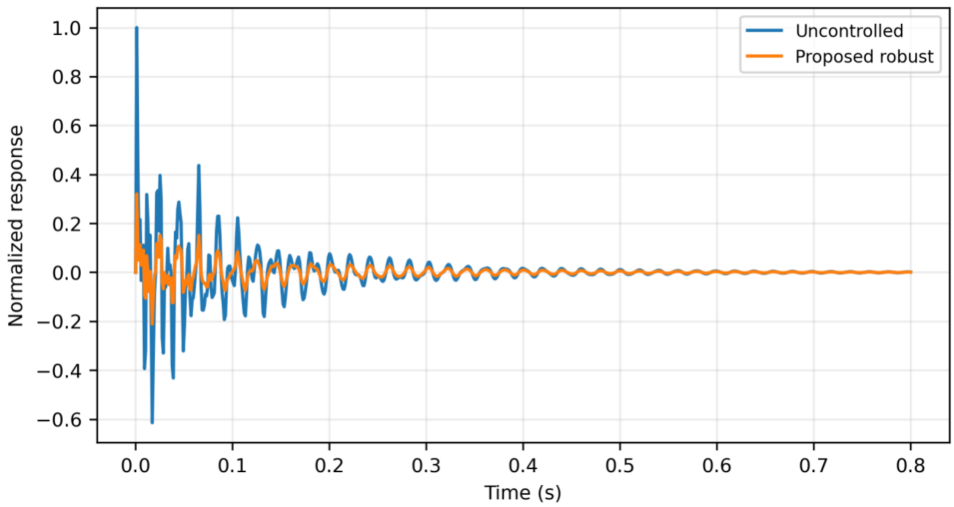

Figure 10. Impulse-response reconstruction from the modal residues of the uncontrolled and optimized systems.

The equal-peak character of the solution is shown in **Figure 11** and quantified in **Table 10**. The tabulated active frequencies were selected as discrete local maxima on the complete 260-point validation grid after optimization; no off-grid interpolation or continuous local-peak refinement was used. In a Chebyshev design, balanced active peaks are preferred to suppression of one peak far below the others, although the spread in **Table 10** also shows that only the leading low-frequency peak is strictly active under the 0.35 dB definition.

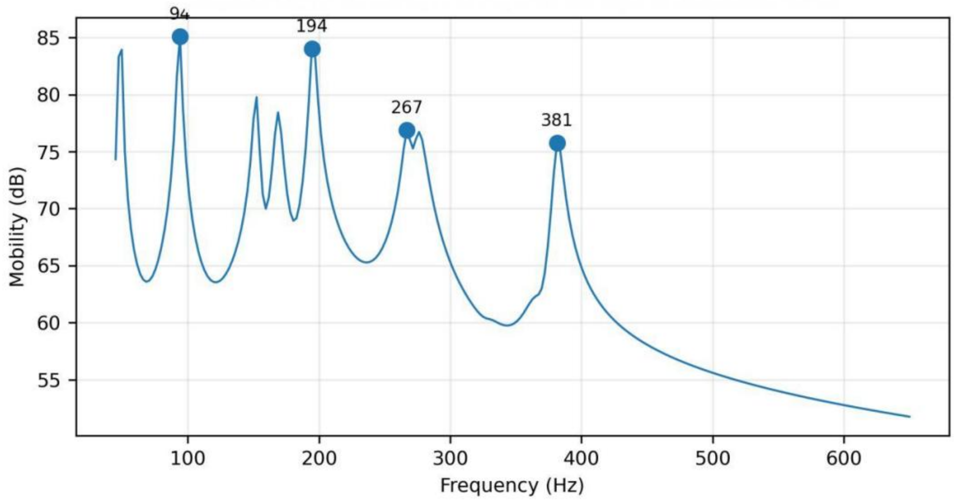

Figure 11. Leading active peaks of the proposed Chebyshev minimax design.

Table 10. Leading active peaks of the proposed robust minimax design.

Active frequency (Hz)	Mobility level (dB)
94.05	85.096
194.50	84.008
266.91	76.886
381.37	75.753

Figure 12 presents the frequency-dependent dynamic stiffnesses of all four branches in the condensed absorber. The shapes differ significantly and objectively express how the mass, damping, and inertance are distributed. This affirms that the final design is a truly networked passive system rather than a repeated single-absorber.

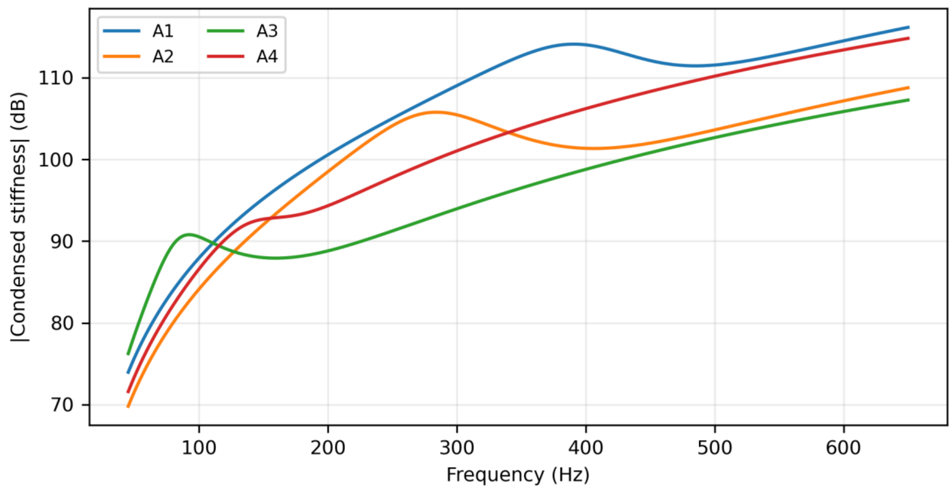

Figure 12. Condensed dynamic-stiffness magnitude of the four optimized absorber branches.

The previous claims in numerical form are gathered in **Table 11** and **Figure 13**. The evidence is intentionally conservative: reporting nominal peak drop, 95th-percentile improvement (a robust statistic), the mean-band difference, and onset shift. The fact that these four indices are judiciously different and the agreement they afford collectively tend to confirm, rather than a single plotted point, that the design concerned improves broadband vibration behaviour.

Table 11. Claim-evidence summary for the optimized mathematical design.

Claim indicator	Numerical evidence
Nominal peak reduction versus uncontrolled	6.793 dB
95th-percentile robust peak reduction versus modal tuning	1.757 dB
Peak reduction versus uniform inerter layout	1.604 dB
Mass ratio used by optimized network	4.200% of plate mass
Worst uncontrolled frequency used for spatial validation	96.390 Hz

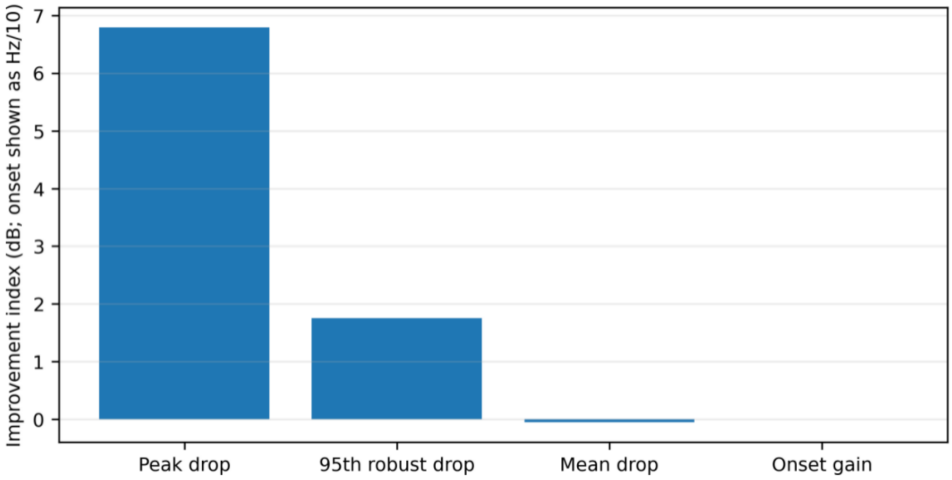

Figure 13. Compact evidence indices for the optimized passive network.

7. Discussion

The calculations illustrate three properties of the design. First, the active peak set is not prescribed: reducing the current maximum can activate a neighbouring resonance, which explains the nonsmooth objective and the need to interpret the unsmoothed form in Equation (25). Second, the nonuniform inertance ratios in **Table 5** supply different apparent-inertia levels at locations with different modal participation; they are functional design variables rather than ornamental additions. Third, the mass-budget curve is non-monotone: the 6.0% case has a lower mean-band level but a higher peak than the selected 4.2% case, confirming that worst-case mobility and average mobility lead to different engineering choices.

The study is intentionally computational and does not claim experimental measurement. The transparent model permits direct inspection of the equations, optimization, and evidence, but it omits joint compliance, installation tolerances, friction, backlash, parasitic mass, and nonideal inertance. **Table 9** indicates that A3 tuning frequency and damping require the tightest control; nevertheless, a dedicated ±5% tolerance analysis is still required. A physical prototype should therefore begin with component identification, followed by impact-hammer or shaker testing, device-envelope verification, and reoptimization with measured parameters.

The approach is not limited to the simply supported plate. The same condensation formulation can be implemented into a finite-element dynamic stiffness matrix, and the same epigraph formulation is applicable for shells, frames, or machine panels. In such a large framework, the matrices in Equations (7) and (20) would not be diagonal anymore, but Equation (33) follows as well. This is a critical point because the mathematical optimization framework generalizes to other types of plate models beyond the specific closed-form model used here for numerical clarity.

8. Conclusion

This study developed a nonsmooth Chebyshev H-infinity framework that coupled a Kirchhoff–Love plate to four condensed passive absorber impedances and optimized mass allocation, tuning frequency, damping ratio, and inertance ratio under a 4.2% mass cap. The reported design reduced nominal peak mobility by 6.793 dB and lowered the 95th-percentile peak by 1.757 dB relative to modal tuning; the mass-budget, sensitivity, and spatial analyses attributed the benefit to redistribution of several modal peaks rather than one isolated resonance.

Future work should first repeat the optimization with 15 and 20 retained modes and document convergence over the full 45–650 Hz band. It should then perform independent seeded runs, include at least ±5% absorber-stiffness and damping tolerances, and enforce device-specific limits on inertance, stroke, force, parasitic mass, and friction. Finally, a manufactured four-node prototype should be identified and validated by shaker or impact-hammer testing before the reported computational advantage is treated as experimentally established.

Author contributions: Conceptualization, YN and AV; methodology, YN; software, YN and PW; validation, YN, RAH and TBNB; formal analysis, YN and PW; investigation, YN, RAH and SIM; resources, AV and TMAF; data curation, YN, PW and TBNB; writing—original draft preparation, YN; writing—review and editing, YN, AV, RAH, PW, TBNB, SIM and TMAF; visualization, YN, PW and TBNB; supervision, AV and TMAF; project administration, YN and AV. All authors have read and agreed to the published version of the manuscript.

Funding: This work received no external funding.

Institutional review board statement: Not applicable.

Informed consent statement: Not applicable.

Data availability statement: All numerical parameters, computed tables, figures, and validation results used for the study are included in the manuscript.

Conflict of interest: The authors declare no conflict of interest.

AI use statement: During the preparation of this work, the authors used ChatGPT (OpenAI) for language verification. The authors subsequently reviewed and edited the content as necessary and take full responsibility for the final content of the published article.

References

1. Smith MC. Synthesis of mechanical networks: The inerter. IEEE Transactions on Automatic Control. 2002; 47(10): 1648–1662. doi: 10.1109/TAC.2002.803532
2. Lazar IF, Neild SA, Wagg DJ. Using an inerter-based device for structural vibration suppression. Earthquake Engineering & Structural Dynamics. 2014; 43(8): 1129–1147. doi: 10.1002/eqe.2390

3. Zuo L, Nayfeh SA. Optimization of the individual stiffness and damping parameters in multiple-tuned-mass-damper systems. Journal of Vibration and Acoustics. 2005; 127(1): 77–83. doi: 10.1115/1.1855929
4. Warburton GB. Optimum absorber parameters for various combinations of response and excitation parameters. Earthquake Engineering & Structural Dynamics. 1982; 10(3): 381–401. doi: 10.1002/eqe.4290100304
5. Nishihara O, Matsuhisa H. Design of a dynamic vibration absorber for minimization of maximum amplitude magnification factor. Transactions of the Japan Society of Mechanical Engineers Series C. 1997; 63(614): 3438–3445. doi: 10.1299/kikaic.63.3438 (in Japanese)
6. Blevins RD. Natural frequency of plates and shells. In: Formulas for Dynamics, Acoustics and Vibration. Wiley; 2015. doi: 10.1002/9781119038122.ch5
7. Boyd S, Vandenberghe L. Convex Optimization. Cambridge University Press; 2004. doi: 10.1017/CBO9780511804441
8. Ben-Tal A, Nemirovski A. Robust convex optimization. Mathematics of Operations Research. 1998; 23(4): 769–805. doi: 10.1287/moor.23.4.769
9. Bertsimas D, Sim M. The price of robustness. Operations Research. 2004; 52(1): 35–53. doi: 10.1287/opre.1030.0065
10. Apkarian P, Noll D. Nonsmooth H-infinity synthesis. IEEE Transactions on Automatic Control. 2006; 51(1): 71–86. doi: 10.1109/TAC.2005.860290
11. Burke JV, Lewis AS, Overton ML. A robust gradient sampling algorithm for nonsmooth, nonconvex optimization. SIAM Journal on Optimization. 2005; 15(3): 751–779. doi: 10.1137/030601296
12. Storn R, Price K. Differential evolution: A simple and efficient heuristic for global optimization over continuous spaces. Journal of Global Optimization. 1997; 11: 341–359. doi: 10.1023/A:1008202821328
13. Rockafellar RT, Wets RJB. Variational Analysis. Springer; 2009. doi: 10.1007/978-3-642-02431-3
14. Bonnans JF, Shapiro A. Perturbation Analysis of Optimization Problems. Springer; 2000. doi: 10.1007/978-1-4612-1394-9
15. Shor NZ. Minimization Methods for Non-Differentiable Functions. Springer; 1985. doi: 10.1007/978-3-642-82118-9
16. Raze G, Kerschen G. H∞ optimization of multiple tuned mass dampers for multimodal vibration control. Computers & Structures. 2021; 251: 106485. doi: 10.1016/j.compstruc.2021.106485
17. Ma R, Bi K, Hao H. Inerter-based structural vibration control: A state-of-the-art review. Engineering Structures. 2021; 243: 112655. doi: 10.1016/j.engstruct.2021.112655
18. Barredo E, Rojas GL, Mayén J, et al. Innovative negative-stiffness inerter-based mechanical networks. International Journal of Mechanical Sciences. 2021; 205: 106597. doi: 10.1016/j.ijmecsci.2021.106597
19. Zhang L, Xue S, Zhang R, et al. A novel crank inerter with simple realization: Constitutive model, experimental investigation and effectiveness assessment. Engineering Structures. 2022; 262: 114308. doi: 10.1016/j.engstruct.2022.114308
20. Cao Y, Li Z, Dou J, et al. An inerter nonlinear energy sink for torsional vibration suppression of the rotor system. Journal of Sound and Vibration. 2022; 537: 117184. doi: 10.1016/j.jsv.2022.117184
21. Alotta G, Biondo C, Giaralis A, et al. Seismic protection of land-based wind turbine towers using the tuned inerter damper. Structures. 2023; 51: 640–656. doi: 10.1016/j.istruc.2023.03.004
22. Barredo E, Zhao Z, Mazón-Valadez C, et al. A grounded inerter-based oscillating TMD for suppressing harmonic and random vibrations. International Journal of Mechanical Sciences. 2023; 254: 108438. doi: 10.1016/j.ijmecsci.2023.108438
23. Rajana K, Wang Z, Giaralis A. Optimal design and assessment of tuned mass damper inerter with nonlinear viscous damper in seismically excited multi-storey buildings. Bulletin of Earthquake Engineering. 2023; 21: 1509–1539. doi: 10.1007/s10518-022-01609-3
24. Cao HQ, Tran NA. Multi-objective optimal design of double tuned mass dampers for structural vibration control. Archive of Applied Mechanics. 2023; 93: 2129–2144. doi: 10.1007/s00419-023-02376-6
25. Li J, Gao T, Zhu S, et al. H∞ optimization of a novel Maxwell dynamic vibration absorber with lever, inerter, and grounded stiffness. Applied Sciences. 2023; 13(6): 3697. doi: 10.3390/app13063697
26. Chillemi M, Furtmüller T, Adam C, et al. Fluid inerter-based vibration control of multi-modal structures subjected to vertical vibration. Engineering Structures. 2024; 307: 117938. doi: 10.1016/j.engstruct.2024.117938
27. Garrido H, Domizio M, Curadelli O, et al. Inerter-based Building Mass Damper: Optimization and experimental study. Engineering Structures. 2024; 301: 117277. doi: 10.1016/j.engstruct.2023.117277

28. Li Y, Zhang Q, Xu Y, et al. Performance evaluation of inerter-based dynamic vibration absorbers for wind-induced vibration control of a desulfurization tower. Buildings. 2024; 14(1): 150. doi: 10.3390/buildings14010150
29. Wu L, Wang K. Optimization design and stability analysis for a new class of inerter-based dynamic vibration absorbers with a spring of negative stiffness. Journal of Vibration and Control. 2024; 30(3–4): 822–836. doi: 10.1177/10775463231151724
30. Zhu YN, Guo XY, Wang Q, et al. A lightweight tuned particle damper for low-frequency vibration attenuation. Journal of Sound and Vibration. 2024; 583: 118440. doi: 10.1016/j.jsv.2024.118440